International Journal of Extreme Manufacturing

Robust and high-sensitivity thermal probing at the nanoscale based on resonance Raman ratio (R3)

OPEN ACCESS
IOP Publishing | IMMT
International Journal of Extreme Manufacturing
Int. J. Extrem. Manuf. 4 (2022) 035201 (12pp)
https://doi.org/10.1088/2631-7990/ac6cb1

Robust and high-sensitivity thermal probing at the nanoscale based on resonance Raman ratio (R3)

Hamidreza Zobeiri[1,4], Nicholas Hunter[1,4], Shen Xu[2,*], Yangsu Xie[3,*] and Xinwei Wang[1,*]

[1] Department of Mechanical Engineering, Iowa State University, Ames, IA 50011, United States of America
[2] School of Mechanical and Automotive Engineering, Shanghai University of Engineering Science, 333 Longteng Road, Shanghai 201620, People's Republic of China
[3] College of Chemistry and Environmental Engineering, Shenzhen University, Shenzhen, Guangdong 518055, People's Republic of China

E-mail: shxu16@sues.edu.cn, ysxie@szu.edu.cn and xwang3@iastate.edu

Received 26 November 2021, revised 13 January 2022
Accepted for publication 4 May 2022
Published 20 May 2022

Abstract

Raman spectroscopy-based temperature sensing usually tracks the change of Raman wavenumber, linewidth and intensity, and has found very broad applications in characterizing the energy and charge transport in nanomaterials over the last decade. The temperature coefficients of these Raman properties are highly material-dependent, and are subjected to local optical scattering influence. As a result, Raman-based temperature sensing usually suffers quite large uncertainties and has low sensitivity. Here, a novel method based on dual resonance Raman phenomenon is developed to precisely measure the absolute temperature rise of nanomaterial (nm WS_2 film in this work) from 170 to 470 K. A 532 nm laser (2.33 eV photon energy) is used to conduct the Raman experiment. Its photon energy is very close to the excitonic transition energy of WS_2 at temperatures close to room temperature. A parameter, termed resonance Raman ratio (R3) $\Omega = I_{A_{1g}}/I_{E_{2g}}$ is introduced to combine the temperature effects on resonance Raman scattering for the A_{1g} and E_{2g} modes. Ω has a change of more than two orders of magnitude from 177 to 477 K, and such change is independent of film thickness and local optical scattering. It is shown that when Ω is varied by 1%, the temperature probing sensitivity is 0.42 K and 1.16 K at low and high temperatures, respectively. Based on Ω, the in-plane thermal conductivity (k) of a ~25 nm-thick suspended WS_2 film is measured using our energy transport state-resolved Raman (ET-Raman). k is found decreasing from 50.0 to 20.0 Wm^{-1} K^{-1} when temperature increases from 170 to 470 K. This agrees with previous experimental and theoretical results and the measurement data using our FET-Raman. The R3 technique provides a very robust and high-sensitivity method for temperature probing of nanomaterials and will have broad applications in nanoscale thermal transport characterization, non-destructive evaluation, and manufacturing monitoring.

[4] These authors contributed equally to this work.
[*] Authors to whom any correspondence should be addressed.

2631-7990/22/035201+12$33.00

Supplementary material for this article is available online

Keywords: resonant Raman scattering, two-dimensional (2D) materials, Raman intensity ratio, ET-Raman, thermal conductivity

1. Introduction

Raman-based methods are among the latest techniques for characterizing the thermal transport properties of two-dimensional (2D) materials, such as graphene, transition metal dichalcogenides (TMDs), and nanowires [1–9]. These methods are used to determine several thermal transport properties, especially thermal conductivity (k) [10, 11]. The steady-state (SS) Raman technique has two main steps to track the temperature response of a 2D material: (a) measurement of laser power (P) dependence of Raman wavenumber (ω) ($\mathrm{d}\omega/\mathrm{d}P$), and (b) measurement of temperature (T) coefficient of ω ($\mathrm{d}\omega/\mathrm{d}T$). Here, the second step works as a calibration tool to find the temperature rise during the laser heating in the first step. The temperature calibration using the measured $\mathrm{d}\omega/\mathrm{d}T$ and measurement of the laser power absorption could introduce significant errors [1]. For instance, laser absorption could vary a lot due to the optical properties variation of unknown samples. An energy transport state-resolved Raman (ET-Raman) technique was developed by Wang's group to overcome the drawbacks of SS Raman by generating steady and transient energy transport states and measuring the Raman shift power coefficient ($\mathrm{d}\omega/\mathrm{d}P$) under each of these states [12–17]. By normalizing the $\mathrm{d}\omega/\mathrm{d}P$ under transient state with its counterpart under SS, a normalized Raman shift power coefficient (Θ) is determined, which is a function of thermal properties of the 2D material. This normalization process eliminates the effects of laser absorption coefficient and Raman shift temperature coefficient measurements. Then, the theoretical Raman intensity weighted average temperature rise under each state is calculated using a three-dimensional (3D) numerical method to determine the theoretical Θ, compare it against the experimental result, and determine a specific property, such as k or hot carrier diffusion coefficient (D) [18, 19].

Each of these techniques, i.e. SS or ET-Raman, uses a specific Raman mode of the material to perform the analysis. Although it was shown that depending on the Raman mode selection, the determined thermal property could be different [20]. For instance, it was shown that the resulting interfacial thermal resistance between a MoS_2 thin layer and quartz substrate is smaller when the E_{2g} Raman mode is used. Also, each of these two main methods needs a considerable amount of time to conduct a large number of Raman measurements to obtain reliable $\mathrm{d}\omega/\mathrm{d}T$ and $\mathrm{d}\omega/\mathrm{d}P$. It could be very time consuming to conduct experiments over a wide temperature range to measure the thermal properties at each environmental temperature. Last but not the least, most of the optothermal techniques based on Raman spectroscopy use indirect approaches to find the temperature rise of the sample under laser irradiation, like finding $\mathrm{d}\omega/\mathrm{d}P$ instead of absolute temperature rise. This is due to the fact that at μm and nm scales, it is hard to track the absolute temperature rise directly using classical methods with sound accuracy.

In this work, a novel technique based on resonance Raman spectroscopy is developed for high sensitivity temperature measurement. It is shown that WS_2 experiences resonance Raman scattering under a 532 nm laser when the Raman experiment is conducted from high to low temperatures, and its two main Raman modes (E_{2g} and A_{1g}) have different intensity variation behaviors against temperature. The intensity ratio of these two modes is found highly sensitive to temperature, and is independent of sample thickness and optical scattering conditions. This provides a remarkable parameter for unprecedented thermal probing. Using this intensity ratio for thermal sensing, k and α of nm-thick WS_2 are obtained at various temperatures from ~170 K to ~470 K without the need of Raman mode selection and laser absorption coefficient. Also, frequency domain ET-Raman (FET-Raman) experiment is conducted for the same sample using both Raman modes and at room temperature (RT) to confirm the measurement results based on Raman mode intensity ratio.

2. Discovery of universal parameter for high sensitivity thermal probing

Here, the two different samples used in this work are prepared using WS_2 and MoS_2 thin films. The WS_2 film will be used for the later on thermal conductivity measurement, and the MoS_2 film is used as a reference of non-resonance Raman scattering. Both films are prepared using mechanical exfoliation from bulk counterparts [21]. Then, each of them is transferred to a silicon (Si) substrate by a gel film and a 3D micro-stage. Thin films are placed over a 5 μm radius hole to create a suspended region. More details of this process and the hole structure can be found in our previous works [17, 22]. Figures S1(a) and (b) (available online at stacks.iop.org/IJEM/4/035201/mmedia) show the atomic force microscopy (AFM) images of these prepared samples. Based on these images, the thickness of WS_2 and MoS_2 films are measured as 25.4 and 61.4 nm, respectively. Also, the root mean square roughness (R_q) of these two samples are measured using these AFM images as 0.96 nm and 1.92 nm, which indicates a uniform contact between the thin film and substrate.

Under laser irradiation with a specific photon energy, the electrons at the ground state of a nm-thick TMD material are excited to a higher energy level (excited state). The energy difference between these two states (ΔE or excitonic transition energy) is a function of temperature [23, 24], and it could be tuned by varying the environment's temperature. Based on the time-dependent perturbation theory explanation of light's polarizability, resonance Raman happens when ΔE is equal

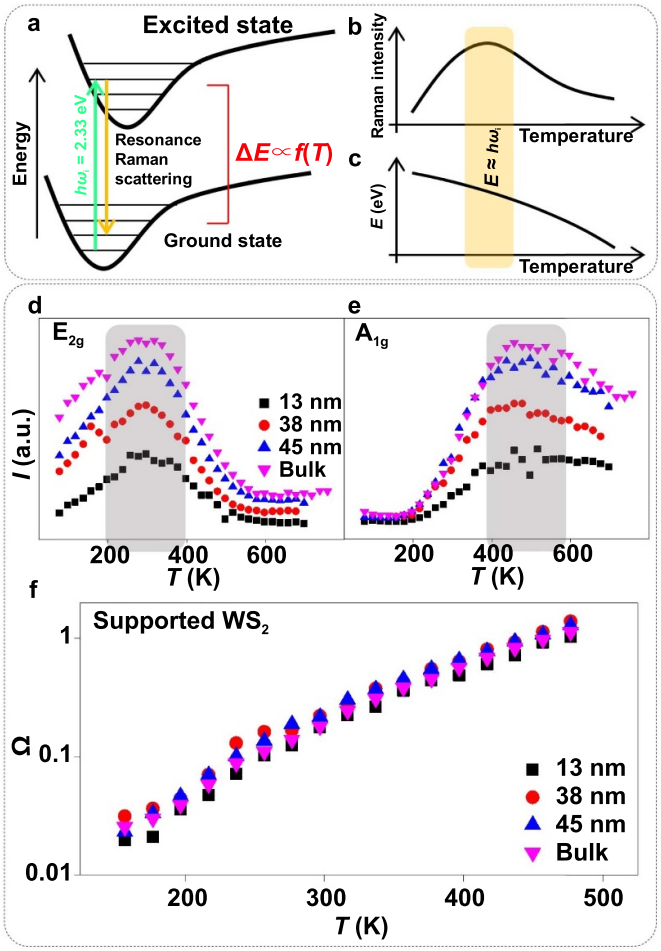

Figure 1. Universal parameter Ω for high sensitivity thermal probing. (a) Resonance Raman happens when the energy of the incident photon is very close or equal to the excitonic transition energy (ΔE), and temperature is one of the main parameters that controls ΔE. (b) Schematic of Raman intensity (I) and (c) excitonic transition energy (E) versus temperature for a WS_2 sample. (d) and (e) Temperature dependent Raman intensity of E_{2g} and A_{1g} modes of all four supported samples, respectively. The gray shaded areas show the temperature range that resonance Raman scattering is very strong. (f) Ω–T plots of supported WS_2 films of various thicknesses.

(or fairly close) to the incident photon's energy ($\hbar\omega_i$), as shown in figure 1(a) [25–27]. According to this theory, the Raman intensity of each mode is related to the incident (E_i) and scattered (E_s) photon energy as [26]:

$$I \propto \left| \frac{1}{[E(T) - E_i - i\Gamma(T)][E(T) - E_s - i\Gamma(T)]} \right|^2. \quad (1)$$

Here, $E(T)$ and $\Gamma(T)$ are the exciton's temperature dependent transition energies and damping constants, respectively. When $E(T)$ is very close to E_i (or E_s), the Raman intensity of the corresponding Raman mode is enhanced significantly. This leads to a significant increase of Raman intensity of the corresponding Raman mode. Figure 1(b) shows this trend of Raman intensity as a function of temperature. When the excitonic transition energy is close to $\hbar\omega_i$, the Raman intensity reaches maximum. Generally, E decreases with the increased temperature for TMD materials and this is explained by the Varshni empirical relationship under resonance condition (figure 1(c)) [23] as $E_B(T) = E_B(0) - \alpha_B T^2/(\beta_B + T)$. Here $E_B(0)$ is the electronic transition energy of B exciton at 0 K. α_B and β_B are Varshni coefficients and are related to the electron (exciton)-phonon interaction and Debye temperature. In this work, a 532 nm continuous-wave (CW) laser (2.33 eV photon energy) is used to excite the Raman signal, and this energy is close to the excitonic transition energy of B exciton of WS_2. The excitonic transition energy of MoS_2 excitons is lower than 2.33 eV over the whole temperature range. Therefore, the MoS_2 sample does not experience any resonance Raman under this laser.

In our previous work [28], a multi-temperature Raman experiment has been conducted for several supported WS_2 samples on Si substrate from 77 to 797 K. AFM images and further information about these four samples could be found in that work. Over this temperature range, we could observe the resonance Raman of all WS_2 sample. Figures 1(d) and (e) represent the result of this Raman experiment for both E_{2g} and A_{1g} modes, respectively. The thicknesses of first three samples were 13, 38, and 45 nm. Also, the thickness of last WS_2 film was more than 200 nm which was considered as bulk. These two plots clearly indicate the resonance Raman scattering of WS_2 under the 532 nm laser for both Raman modes. For each Raman mode, we can obviously see that the I–T curve is different from sample-to-sample. Here, I is the normalized Raman intensity by the laser power and integration time. This difference is related to multiple factors, such as different interfacial spacing between WS_2 and Si, film thicknesses, variation of local optical interference, and different film profile changes against temperature. These figures also indicate that the Raman intensity of E_{2g} mode reaches its maximum value at a lower temperature than the A_{1g} mode. This was attributed to several reasons. First, the acoustic 2LA(M) mode is very close to the E_{2g} mode, and it is relatively strong at low temperatures. Therefore, it can slightly affect the peak fitting at those temperatures. Second, the effects of thermal expansion on Raman modes are different, and it has been observed that the A_{1g} mode is more sensitive to this effect [28–30]. Another factor could be the variation of optical properties of thin-film due to experimental temperature change. The refractive index of WS_2 film at wavelengths related to each Raman mode is different and could be another factor that contributes to this difference among I–T trends. Another key point is that E_{2g} and A_{1g} modes have different excitonic temperatures. Each of these two Raman modes shows different temperature dependent behaviors. Even for a similar peak, the I–T curves vary from sample to sample. Very surprisingly, the ratio of intensity of these two modes, here termed as resonance Raman ratio Ω defined as: $\Omega = I_{A_{1g}}/I_{E_{2g}}$, is identical for all four samples regardless of their structural differences. This new parameter reflects the combined effects of temperature on excitonic energies and the resulting Raman resonance extent. Note the bulk material used here has a very smooth surface and this surface is used in testing. The curve shown in figure 1(f) will

not be affected by surface roughness since this roughness will have the same effect on E_{2g} and A_{1g} peaks, and their ratio $\Omega = I_{A_{1g}}/I_{E_{2g}}$ completely eliminates this effect.

Figure 1(f) indicates this observation for all the four supported WS_2 samples for temperature range of 177–477 K. Our key conclusion is that all the samples follow the same curve (Ω) regardless of the thickness, proving Ω is universal and can be used for thermal probing of samples regardless of their thicknesses, structures, and the varied local optical scattering. It is observed when temperature changes from 177 to 477 K, Ω changes by around two orders of magnitude. This strongly demonstrates the potential of using Ω for very high sensitivity temperature measurement. Based on this analysis, when Ω is varied by 1%, the temperature probing sensitivity is 0.46 K and 1.24 K at 177 K and 477 K, respectively. This strongly confirms the high precision of temperature probing using Ω.

3. Thermal transport characterization using Ω

3.1. Physical principles

In this section, we perform thermal transport characterization of 2D materials using thermal probing based on Ω. Here, two heating stages are designed to characterize the temperature rise of the nm-thick WS_2 sample based on the resonance Raman. The first one is the calibration stage in which the WS_2 film is supported on a Si substrate (right-hand side of figure 2(a)). The Raman intensity of E_{2g} (or A_{1g}) mode of this sample is collected from low to high temperatures under a low heating power laser. The laser power is minimized to prevent any additional significant temperature rise by laser heating. Here, the two main Raman modes of WS_2 are studied (E_{2g} and A_{1g}), and their Raman intensity is collected during the experiments. Figure 2(b) shows I–T and Ω–T plots schematically. This calibration is intended to build the Ω–T correlation. Then the obtained Ω–T correlation is used as the reference to measure the temperature rise of WS_2 under the other stage: suspended sample. Note in the calibration stage, the sample experiences optical interference within the sample and the sample-substrate spacing while the suspended sample only experiences optical interference within it. However, this will not cause errors in using the Ω–T correlation to measure temperatures of suspended samples. This is because the interference-caused intensity change will be completely eliminated in Ω calculation since it has very close effects on both E_{2g} and A_{1g} peak intensities. This point can also be readily proved by the same Ω–T relation shown in figure 1(f) for different-thickness samples that have very different optical interference within them. The suspended stage is shown in figure 2(a) (left hand-side). The WS_2 film is suspended over a hole, and is irradiated by using the same 532 nm laser and same objective lens (i.e. similar local heating area). This sample experiences a higher temperature rise caused by laser heating due to its suspended structure (larger thermal resistance), and its I–T curve reaches the maximum value at a lower temperature compared with the supported film. This is shown with the red curve in figure 2(b). Also, the Ω–T plot for this stage will take larger values compared with the calibration stage (figure 2(b)). As a result, the absolute temperature rise of the suspended WS_2 film (ΔT) is measured directly by comparing these two curves at each similar Ω. Note that the temperature rise of the supported WS_2 due to the local laser heating is minimal. This is because of the very high thermal conductivity of Si substrate.

Next, a frequency domain energy transport state-resolved Raman (FET-Raman) technique is used to characterize the thermal conductivity of the thin film. This technique consists of two heating stages: (a) SS (CW) under the CW laser, and (b) the transient state (F) under the amplitude modulated (f) CW laser (figure 2(c)). The multi-temperature resonance Raman experiment is conducted for both stages, and the temperature rise of the thin film (ΔT_{CW} and ΔT_F) is measured by comparing it to the calibration stage (i.e. supported sample). For both the CW and F states, the sample is excited and heated with the same laser of 532 nm wavelength. The temperature rise under each state is evaluated using their Ω. Note that the temperature rise under the CW stage is more than the transient one, and their multi-temperature Raman intensity curve will not be identical, as shown in the topright panel of figure 2(c). Based on this, a new experimental parameter (Θ) is obtained as: $\Theta = \Delta T_F/\Delta T_{CW}$. By performing this ratio calculation, the effects of laser power absorption and Raman intensity temperature coefficient ($\partial I/\partial T$) measurements are eliminated. Also, there is no effect of Raman peak selection on our analysis by obtaining Ω. Based on this analysis, Θ is only a function of k and ρc_p. Next, 3D numerical calculation based on the finite volume method is conducted to determine the temperature rise of the suspended thin film and find k at each temperature based on the results of the resonance Raman experiment (see section 5.2 for more information about this calculation). Since the ρc_p of the thin film is a function of temperature, the exact ρc_p at each specific temperature (from references) is used in our numerical modeling to calculate the theoretical temperature rise. The theoretical Θ (Θ_{th}) is found using the calculated temperature rise under two heating stages as a function of k, and k at each environmental temperature (T) is determined by interpolating this curve against the measured Θ from resonance Raman experiment (figure 2(d)). The classical FET-Raman measurement (see section 5.3 for more information about this technique) is also conducted at RT for a similar WS_2 sample to compare with resonance Raman experiment results [31, 32]. This technique uses the Raman wavenumber shift to probe the temperature rise and measure thermophysical properties.

3.2. Multi-temperature resonance Raman experiment

The multi-temperature Raman experiment is conducted for both WS_2 and MoS_2 samples from 170 to 470 K. Over this temperature range, we could observe the resonance Raman of the WS_2 sample for all three heating stages: Supported (or calibration), CW, and transient (F). This is shown in figures 3 and S2. Figures 3(a) and (b) show the 2D Raman intensity contour of suspended WS_2 under CW and F states over this temperature range. The same contour for the calibration stage is presented in figure S2. For all Raman experiments conducted in this

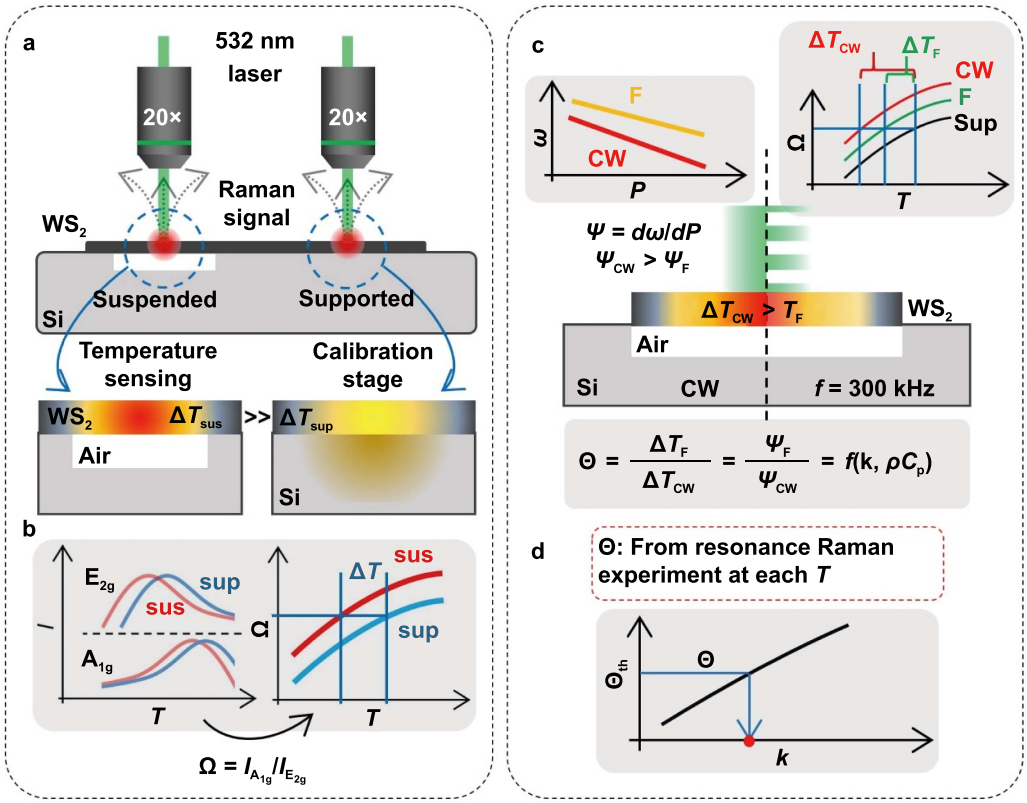

Figure 2. Physical principles of multi-temperature resonance Raman and FET-Raman techniques. (a) Heating stages of the multi-temperature resonance Raman experiment. The supported sample works as the calibration stage, and a 532 nm laser is used to excite the Raman signal. The objective sample is suspended over a hole and experiences a higher temperature rise under laser irradiation. A 20× objective lens is used to perform the Raman experiment. (b) Schematic of I and Ω versus temperature for two heating stages. The absolute temperature rise of the suspended WS_2 (ΔT) is determined by comparing Ω curves of this state with the calibration one. (c) Schematic of the FET-Raman experiment. The top left of this figure shows the redshift of Raman wavenumber of each Raman mode of WS_2 versus laser power under both CW and transient (c) stages. The top right of this figure represents the determined temperature rise of the suspended WS_2 under CW and F states using the multi-temperature resonance Raman experiment schematically. (d) Thermal conductivity (k) of WS_2 at each temperature is determined using the theoretical value of Θ and its experimental counterpart from the resonance Raman experiment.

work, a 20× objective lens with a radius (r_0) of ∼2.02 μm is used. Figure S1(c) shows the laser intensity distribution under this objective, and this figure is analyzed to find r_0.

Here, the CW laser amplitude is modulated at 300 kHz frequency to construct the F state experiment (more details about this frequency selection in section 5.3). The Raman intensity of both modes is lower under F state than CW for the suspended sample, and this is due to the pulsed heating under F state. Note that the on-time laser power of F state is similar to the CW laser power. I of both modes and three states are shown in figure 3(c). This figure clearly shows the non-monotonic behavior of I versus temperature. Ω under each state is calculated and plotted as figure 4(a) for all three stages. The blue curve corresponds to the calibration with zero local temperature rise, and it is shown that Ω takes larger values for the suspended sample. Here, the Ω is plotted versus T to show this effect more clearly. Next, the Ω of calibration stage is fitted using an allometric function (solid lines in this figure) as: $\Omega = aT^b$, where a and b are the fitting parameters corresponding to the supported (calibration) stage. Here, the universal parameters a and b are 5.088×10^{-11} and 3.860, respectively. This function is used to determine the temperature rise (ΔT) of the CW and F states at each T. Figure 4(b) shows the result of this analysis (left axis), and it indicates an increasing trend of ΔT versus T under both stages. Also, the solid lines represent the fitting of each ΔT–T plot. Note this fitting is pure data processing to guide eyes and show the data trend. The right vertical axis of this plot shows the experimental Θ values, and it decreases with the increased temperature. Note that one of the Θ values in this plot is larger than 1 (at ∼190 K), and this is caused by the experimental or fitting uncertainties at very low temperatures. Again, the solid green line shows the Θ calculated from the fitted ΔT values (black and solid red lines). As shown in figure 3(c), the Raman intensity of A_{1g} mode at low T is fairly small. This could lead to some uncertainties when fitting this peak. These Θ values are used to determine the thermal conductivity of the WS_2 sample.

Over a similar temperature range, the MoS_2 sample does not experience any resonance Raman because its excitonic transition energy (∼1.8 eV) is below the incident photon energy (2.33 eV) [26, 33, 34]. Figure S3 shows the 2D contours of Raman intensity of both modes of MoS_2 for a supported (figure S3(a)) and a suspended (figure S3(b)) region. The extracted Raman intensities of each mode are plotted in

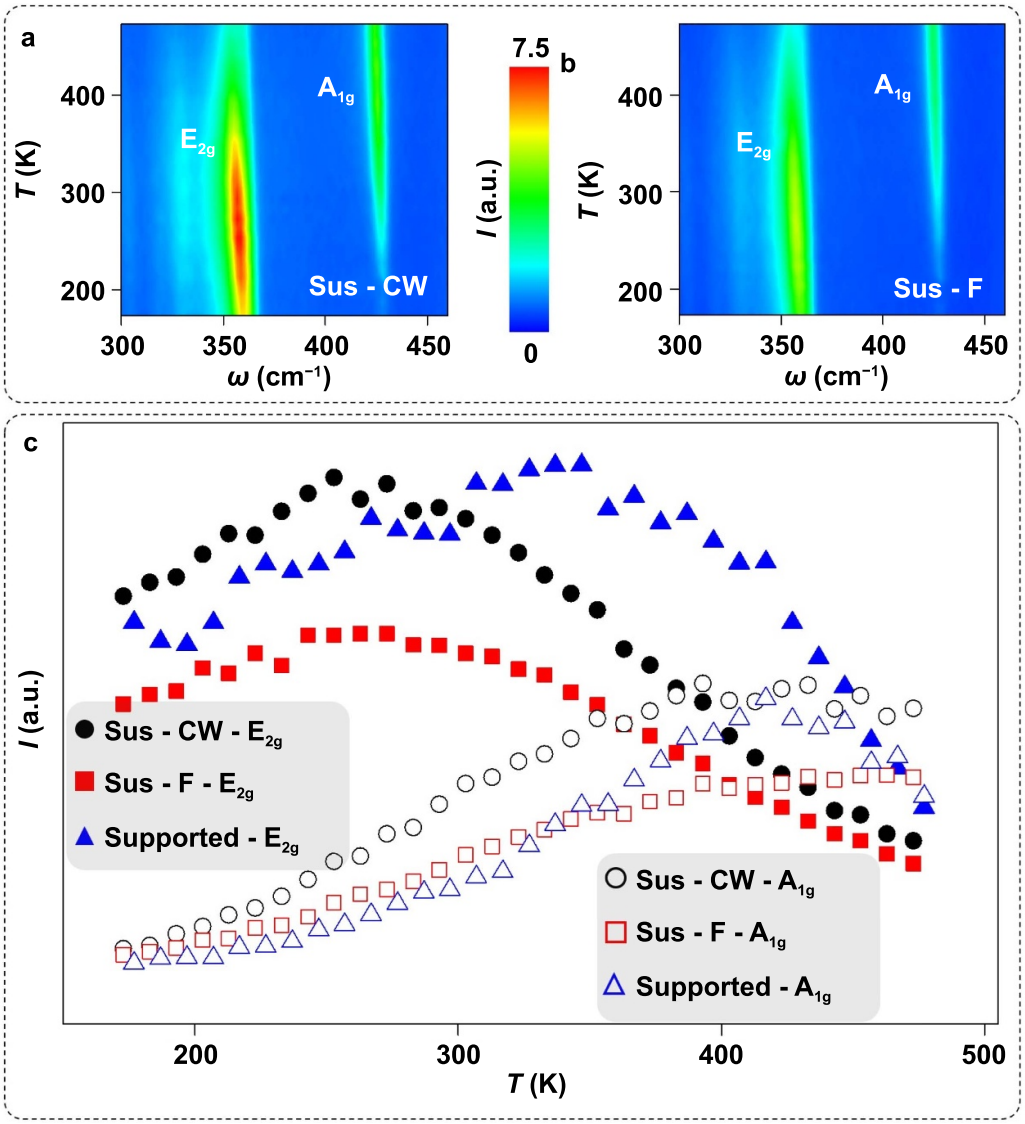

Figure 3. Experimental results of multi-temperature resonance Raman measurement. (a) and (b) 2D contours of I of suspended WS_2 under CW and F states, respectively. These contours show the redshift of each Raman mode with the increased T. (c) I–T plots for all three stages of WS_2 films and their two Raman modes. This plot shows a distinct difference between the resonance behavior of the suspended region and the supported one, similar to the results of figure 1(e). The laser power just before entering the thin film is 3.85 mW, and the integration time is 5 s in Raman experiment.

figures S4(a) and (b) for both regions, and the resultant Ω–T is shown in figure S4(c). This plot clearly shows that Ω takes a constant value of $\sim$2.2 for the supported MoS_2 film. The data corresponding to the suspended region is noisier and it could be related to the Raman peak fitting uncertainties caused by lower Raman intensity of both modes at low temperatures in this region.

3.3. Thermal conductivity and diffusivity determination

To determine the thermal properties of WS_2 thin film, a 3D numerical calculation based on the finite volume method is conducted and coupled with the experimental results, which were discussed in previous sections (see section 5.2 for details of this calculation). The theoretical temperature rise of the suspended WS_2 film under both states ($\Delta T_{CW,th}$ and $\Delta T_{F,th}$) is calculated using the known ρc_p values at each experimental temperature for a wide range of thermal conductivity. Then, the theoretical normalized temperature rise (Θ_{th}) is found as: $\Theta_{th} = \Delta T_{F,th}/\Delta T_{CW,th}$. Figure S5 shows the c_p and ρ that are used to perform this calculation [35]. The red solid line in figure S5 shows the fitted c_p values using the Debye model of specific heat. The inset of figure 5 shows the result of this calculation. The y-axis of this 2D contour is the environmental temperature which corresponds to each ρc_p value in our numerical simulation. The solid line inside this contour corresponds to Θ_{th} value of 0.81, which is the experimental Θ at 303 K (as shown in figure 4(b)), and two dashed lines represent the uncertainty of this experimental value. Using this contour, the thermal conductivity and its uncertainty are determined at each temperature. The main plane of this figure shows each of these contour lines at three specific temperatures to indicate

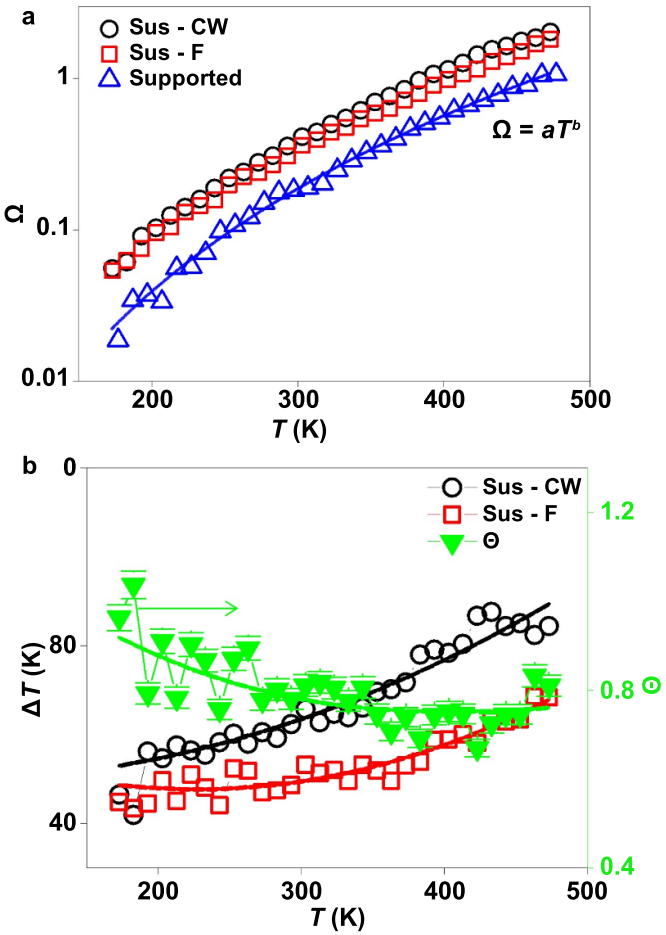

Figure 4. Normalized Raman intensity of suspended and supported WS_2. (a) The solid blue line is the fitting result as the reference used to find the temperature rise of the suspended sample. Note the vertical axis is in log scale. (b) The measured temperature rise of suspended WS_2 (left vertical axis) and normalized temperature rise (right vertical axis). Θ takes values close to ∼ (0.7–0.8) which is related to the 300 kHz frequency of the transient state.

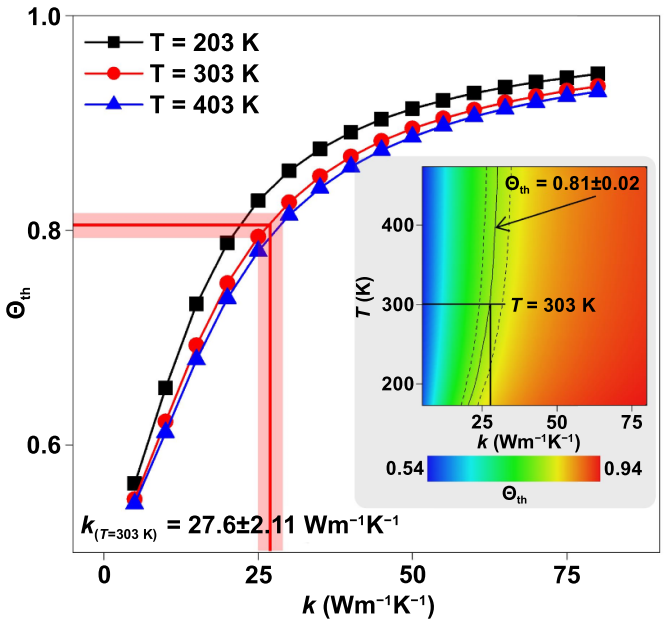

Figure 5. Thermal conductivity determination at each environmental temperature. Each of these three curves shows the theoretical calculated Θ at a specific temperature as a function k, and k at each T is found by interpolating these curves with the corresponding experimental Θ from the multi-temperature resonance Raman experiment. The inset of this figure shows the 2D contour of Θ_{th} that is calculated at all related temperatures and k.

this process more clearly. The determined k at all temperatures is shown in figure 6(a). Larger fluctuations are observed at lower temperatures. This is due to the fluctuations of Θ_{exp} at this temperature range (figure 4(b)). However, at temperatures larger than 273 K (shown by a gray rectangle), k takes values with an average of ∼25 Wm^{-1} K^{-1}. The solid black line is the k determined using the fitted Θ values from figure 4(b) and shows a clear decreasing trend of k with the increased T. Part (b) of this figure shows the determined thermal diffusivity (α) of this sample as a function of temperature (left vertical axis). Also, ρc_p values that are used to find α are plotted in this figure (right vertical axis).

3.4. Room temperature thermal conductivity measurement using FET-Raman

In this section, k of WS_2 film is measured at RT using the FET-Raman technique, in order to compare with and assess the measurement accuracy of resonance Raman discussed above. Figure 2(c) shows the physics of FET-Raman (topleft panel). Under both CW and F states, the Raman shift power coefficient (ψ_F and ψ_{CW}) is measured: $\psi = d\omega/dP$. Here, ω and P are Raman wavenumber of E_{2g} (or A_{1g}) mode and laser power, respectively. Obviously, the absolute value of ψ_{CW} is larger than ψ_f due to the SS heating nature of CW stage, which shows the higher temperature rise of the suspended film. Based on these two values, the normalized Raman shift power coefficient is determined as: $\Theta_{FET\text{-}Raman} = \psi_F/\psi_{CW}$. Note that $\Theta_{FET\text{-}Raman}$ is theoretically equal to the normalized temperature rise that was defined in previous sections (see section 5.3 for more details about FET-Raman technique). Again, $\Theta_{FET\text{-}Raman}$ is a function of k and ρc_p.

Figures 7(a) and (b) show the 2D contour of Raman intensity of WS_2, two main peaks as a function of P for CW20 and F20 states, respectively. Note that here the 20× objective lens is used to perform the Raman experiment. These contours indicate the redshift of each mode as laser power takes larger values. Each of these Raman spectra is fitted, and the peak location is obtained to find the experimental values of ψ under both states. Figure 7(c) shows the result of this analysis, and each set of data is fitted using a linear function to find ψ. Based on these values, $\Theta_{FET\text{-}Raman}$ using E_{2g} and A_{1g} modes are obtained as 0.766 ± 0.012 and 0.806 ± 0.017, respectively. Then, using these two values and the result of our numerical simulation (figure 5) at RT, k is found by using each Raman mode. This is shown in figure 7(d). For E_{2g} and A_{1g} modes, k is found as 21.8 ± 1.36 Wm^{-1} K^{-1} and 26.3 ± 3.26 Wm^{-1} K^{-1}, respectively.

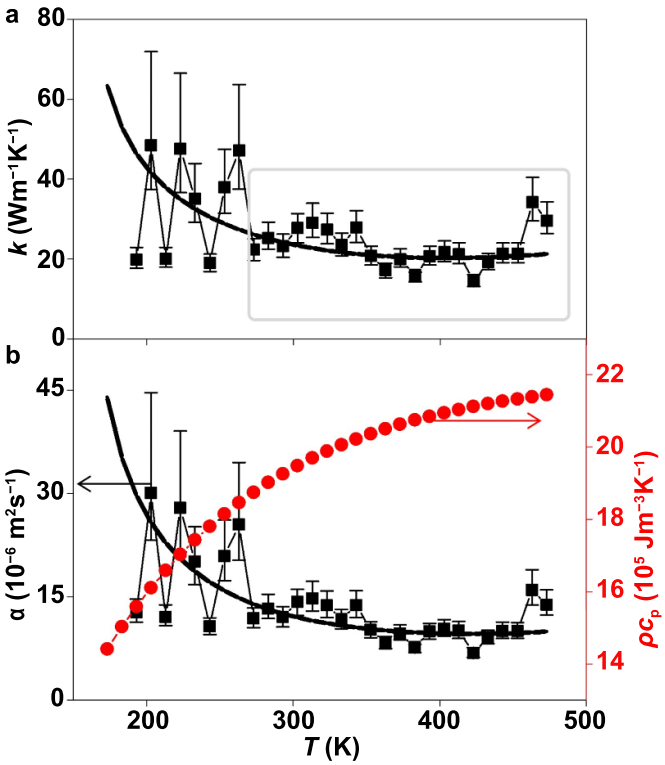

Figure 6. Determined thermal conductivity and diffusivity. (a) k and (b) α of WS_2 at various temperatures. The right vertical axis of figure (b) shows the temperature-dependent ρc_p used in this work to find α based on the measured k.

3.5. Discussion

The measured k at RT using the multi-temperature resonance Raman is 23.2 $\pm$ 2.88 Wm^{-1} K^{-1} (figure 6(a)), and is very close to the result of the FET-Raman experiment at RT (section 3.4). This clearly indicates the accuracy of the multi-temperature resonance Raman technique. As shown in figure 6(a), k of WS_2 sample decreases with the increased temperature, which indicates that the Umklapp scattering mechanism dominates phonon scattering [36, 37]. This is consistent with the theoretical calculation of k of WS_2 conducted by Huang *et al* [38]. It was shown in their work that k of WS_2 is decreased from 32 Wm^{-1} K^{-1} at RT to 23 Wm^{-1} K^{-1} at 600 K.

Our novel multi-temperature resonance Raman technique possesses several advantages over classical optothermal techniques. First, the absolute temperature rise of the sample is measured in this method, instead of characterizing the temperature rise indirectly using the Raman shift power coefficients or direct temperature sensing using a thermocouple which introduces significant errors to temperature measurement. The Raman spectra of both E_{2g} and A_{1g} peaks are obtained in the same measurement, so their intensity ratio eliminates all the effects induced by optical focusing, laser powers, detection, and optical interference since all these have the same effects on these two peaks. If a material has defects that cause change in its excitonic energy variation with temperature, this can be considered by calibrating Ω change with T. The material used in this work: WS_2 has very weak anisotropy, therefore variation of the incident laser polarization with respect to the material's structure has negligible effect on T measurement. For strongly anisotropic 2D materials, we can either use a non-polarized laser source for Raman excitation or use a fixed angle between the crystographical orientation and the laser polarization to obtain reliable temperature measurement. Second, the measured thermal property, like k or interfacial thermal resistance, is independent of the Raman mode selection. Note that each Raman mode is related to a specific optical phonon branch, and these branches experience different temperature rises under a similar heating condition. This effect is studied in detail in our previous work, and it was shown that interface thermal resistance is different among phonon modes of a supported MoS_2 film [20]. Another advantage of this method is that there is no need for Raman shift temperature coefficient calibration and laser absorption measurement. These two factors are the main sources of errors of the SS Raman technique. Last but not least, the experimental procedure takes a much shorter time compared with previous techniques, and it is possible to run several experiments in a shorter period of time.

This technique could have several other applications besides measuring the thermal conductivity of suspended 2D materials. For instance, WS_2 could be used as a thermal sensor to measure the temperature rise of another 2D material that is not experiencing resonance Raman. Also WS_2 can be deposited on other non-Raman active materials to measure their temperature with high accuracy and spatial resolution [39]. In this work, the suitable temperature range of measurement depends on how the excitonic energy varies with temperature. The sensitivity can be tuned by using a Raman excitation laser

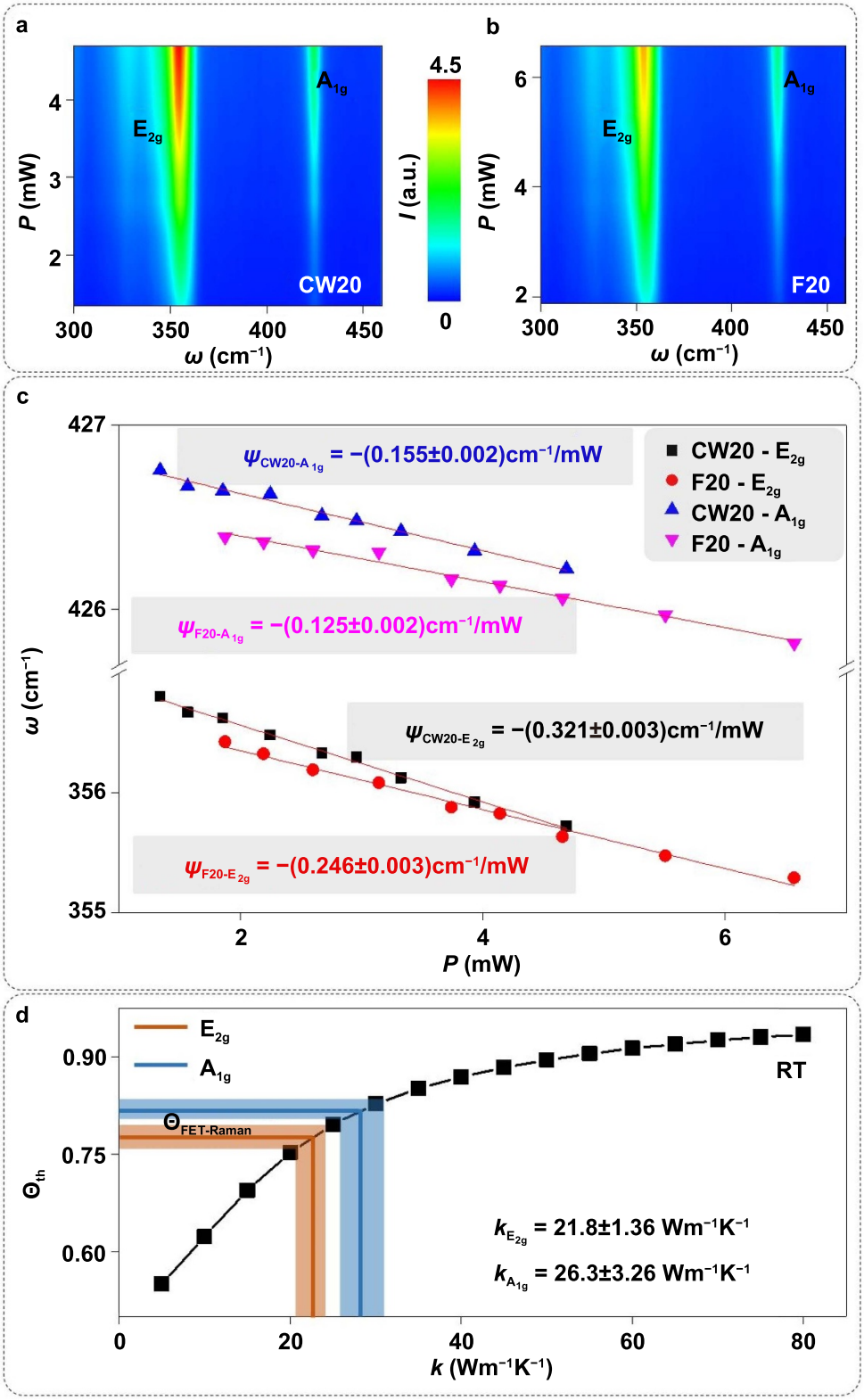

Figure 7. Results of FET-Raman experiment at RT. (a) and (b) 2D contour of *I* of WS_2 sample under various laser powers for CW20 and F20 states, respectively. (c) Measured Raman shift power coefficient using E_{2g} and A_{1g} modes. (d) Determined *k* of suspended WS_2 using the FET-Raman technique and both Raman modes at RT.

of different wavelength or using another material of different resonance Raman behavior. For example, it was shown by Fan *et al* that MoS_2 samples experience similar resonance Raman behavior when a 633 nm wavelength laser is used to excite the Raman signal. This is due to the lower excitonic transition energy of MoS_2 (∼2.06 eV) compared with WS_2 [26].

4. Conclusion

A novel resonance Raman ratio (R3) method was developed for high sensitivity temperature measurement at the nanoscale. For WS_2 studied in this work, the resonance Raman ratio $\Omega = I_{A_{1g}}/I_{E_{2g}}$ changes by two orders of magnitude from 177 to 477 K, demonstrating a very high sensitivity. For example, under RT experimental conditions, 1% change in Ω will lead to a temperature probing sensitivity of 0.78 K, superior over Raman wavenumber-based temperature probing. Also Ω was found intendent of local optical scattering conditions that could be altered by temperature, local structure profiles, and optical focusing level. Using the R3 technique, the thermal conductivity of a suspended WS_2 sample was measured from 170 K to 470 K by directly evaluating the laser-induced temperature rise under CW and periodically modulated laser heating. The result of this experiment at RT was verified with the results of classical FET-Raman technique that uses the Raman wavenumber shift for thermal probing. Also, it was shown that the ET-Raman based on R3 thermal probing eliminates the errors caused by laser absorption measurement and Raman shift temperature coefficient calibration. These are some of the main sources of error in reported optothermal techniques based on Raman spectroscopy. The R3 technique could be applied to other materials with appropriate laser wavelength selection to measure the temperature rise in a wide temperature range, or to characterize their thermal properties, such as thermal conductivity and interfacial thermal resistance.

5. Methods

5.1. Raman spectroscopy measurement

The Raman system used in this work consists of a 532 nm continuous wave (CW) laser (Excelsior-532-150-CDRH, Spectra-Physics), a Raman spectrometer (Voyage, B&W Tek, Inc.), an electro-optics frequency modulator (EOM), a microscope (Olympus BX53), and a multi-temperature environment cell chamber. The laser power is controlled using a motorized neutral density filter which is controlled by LabView software. More information about this Raman system could be found in our previous works [13, 40–42].

5.2. 3D numerical modeling for temperature calculation

The theoretical calculation of temperature rise was conducted using 3D numerical modeling based on the finite volume method. To do so, the actual size of the sample and its thickness, as well as the real laser spot radius (r_0) measured from the Raman experiment were used to calculate the temperature rise under each heating state (CW or F). The governing equations are:

$$\rho c_p \frac{\partial \Delta T}{\partial t} = k \frac{1}{r}\frac{\partial}{\partial r}\left(r\frac{\partial \Delta T}{\partial r}\right) + k_\perp \frac{\partial^2 T}{\partial z^2} + \dot{q}, \tag{2}$$

$$\dot{q}(r,z) = \frac{I_0}{\tau_L}\exp\left(-\frac{r^2}{r_0^2}\right)\exp\left(-\frac{z}{\tau_L}\right). \tag{3}$$

Here ρc_p, k, $k_\perp$, $\dot{q}$, I_0 ($= 1\,\mathrm{mW}/\pi r_0^2$), and τ_L are volumetric heat capacity, in-plane thermal conductivity, out-of-plane thermal conductivity, volumetric Gaussian beam heating, unit laser power per unit area, and laser absorption depth of the thin film. For ease of derivation, here we use the form of $\exp(-r^2/r_0^2)$ instead of the traditional $\exp\left[(-r^2/(2r_0^2)\right]$ to express our Gaussian beam energy distribution in the radial direction. This will not affect our results as we follow the same form in both modeling and experimental data processing. τ_L is calculated as: $\tau_L = \lambda/4\pi k_L$, where λ and k_L are laser wavelength (here 532 nm) and extinction coefficient of WS_2/MoS_2. For WS_2 and MoS_2, τ_L is 47.1 and 36.5 nm, respectively [43–46]. Although τ_L affects the absolute value of temperature rise under each state, the normalized temperature rise (Θ) is almost independent of the τ_L value in our technique. This is well illustrated in our previous work [15]. Note that under CW state, the left-hand side of equation (2) is equal to zero. Using these two equations, the temperature rise (T) at each location (r, z) is obtained. Next, the Raman-intensity weighted average temperature rises (ΔT_{CW} and ΔT_F) are determined as: $\int_0^V Ie^{-z/\tau_L}T\mathrm{d}v / \int_0^V Ie^{-z/\tau_L}\mathrm{d}v$ and $\int_0^t\int_0^V Ie^{-z/\tau_L}T\mathrm{d}v\mathrm{d}t / \int_0^t\int_0^V Ie^{-z/\tau_L}\mathrm{d}v\mathrm{d}t$, for CW and F states, respectively. Here, V is the volume of the sample, and the term e^{-z/τ_L} represents the Raman signal attenuation when the signal leaves the scattering location. Also, I is the laser heating source which was shown by $\dot{q}$ in equation (3). Finally, the normalized theoretical temperature rise is calculated as: $\Theta_{th} = \Delta T_F/\Delta T_{CW}$. In our modeling, the surface reflectivity is not considered. This will not affect our Θ_{th} calculation since it only depends on the ratio of temperature rise under CW and F states.

5.3. Physics of FET-Raman

The RT FET-Raman technique was first developed and introduced by Wang's group [31, 32, 47, 48]. In this method, the 2D material sample is irradiated under two modes of SS and frequency-modulated transient state. The sample's temperature rise under the transient state depends on the modulation frequency, and it was shown that the temperature rise ratio (transient state divided by SS) takes a value in the range of ~0.5–1 [31]. Note that the transient state is created by modulating the same CW laser using a square wave function. Therefore, the heating and cooling (or laser on-time and off-time) periods under transient state are identical. The accuracy of FET-Raman is maximum when the temperature rise ratio is ~0.75. To find the ratio of local temperature rise, the Raman shift power coefficient (ψ) is collected under both states as: $\psi_{SS} = \partial\omega/\partial P \propto \alpha(\partial\omega/\partial T)f_1(k)$ and $\psi_{Transient} = \partial\omega/\partial P \propto \alpha(\partial\omega/\partial T)f_2(k, \rho c_p)$ (Top left of figure 2(c)). Next, the normalized Raman shift power coefficient is found as: $\Theta = \psi_{Transient}/\psi_{SS} \propto f_2(k, \rho c_p)/f_1(k)$. This normalized parameter is equal to the normalized temperature rise of the sample under laser irradiation, i.e. $T_{Transient}/T_{SS}$, where T_{SS} and $T_{Transient}$ are the local temperature rises of the thin film under CW and amplitude modulated laser, respectively. In this work, a 300 kHz frequency is used to modulate the CW laser,

and it was shown by figures 5 and 7 that experimental Θ is around $\sim$0.75, which guarantees the high accuracy performance of FET-Raman. These expressions are related to a suspended sample structure. If the sample is supported over a substrate, each of them will depend on the interfacial thermal resistance too. Therefore, the FET-Raman is capable of measuring the interfacial thermal resistance, as shown in our previous works. Also, by doing this calculation, the effects of laser absorption measurement are totally eliminated in our analysis, which is one of the main sources of error in optothermal techniques based on Raman spectroscopy.

Acknowledgments

Support of this work by National Science Foundation (CBET1930866 and CMMI2032464 for X W) and National Natural Science Foundation of China (No. 52106220 for S X and No. 51906161 for Y X) is gratefully acknowledged.

Conflict of interest

All authors have no competing interests to declare.

ORCID iD

Xinwei Wang https://orcid.org/0000-0002-9373-3750

References

[1] Malekpour H and Balandin A A 2018 Raman-based technique for measuring thermal conductivity of graphene and related materials *J. Raman Spectrosc.* **49** 106–20
[2] Xu S, Fan A, Wang H, Zhang X and Wang X 2020 Raman-based nanoscale thermal transport characterization: a critical review *Int. J. Heat Mass Transfer* **154** 119751
[3] Wang R, Xu S, Yue Y and Wang X 2020 Thermal behavior of materials in laser-assisted extreme manufacturing: Raman-based novel characterization *Int. J. Extreme Manuf.* **2** 032004
[4] Sett S, Aggarwal V K, Singha A and Raychaudhuri A K 2020 Temperature-dependent thermal conductivity of a single Germanium nanowire measured by Optothermal Raman Spectroscopy *Phys. Rev. Appl.* **13** 054008
[5] Hajidavalloo M R, Shirazi F A and Mahjoob M J 2020 Performance of different optimal charging schemes in a solar charging station using dynamic programming *Optim. Control Appl. Methods* **41** 1568–83
[6] Xie Y, Han M, Wang R, Zobeiri H, Deng X, Zhang P and Wang X 2019 Graphene aerogel based bolometer for ultrasensitive sensing from ultraviolet to far-infrared *ACS Nano* **13** 5385–96
[7] Gao J, Zobeiri H, Lin H, Xie D, Yue Y and Wang X 2021 Coherency between thermal and electrical transport of partly reduced graphene paper *Carbon* **178** 92–102
[8] Velson N V, Zobeiri H and Wang X 2020 Rigorous prediction of Raman intensity from multi-layer films *Opt. Express* **28** 35272–83
[9] Xie Y, Zobeiri H, Xiang L, Eres G, Wang J and Wang X 2021 Dual-pace transient heat conduction in vertically aligned carbon nanotube arrays induced by structure separation *Nano Energy* **90** 106516
[10] Sahoo S, Gaur A P S, Ahmadi M, Guinel M J F and Katiyar R S 2013 Temperature-dependent Raman studies and thermal conductivity of few-layer MoS_2 *J. Phys. Chem.* C **117** 9042–7
[11] Lin H, Wang R, Zobeiri H, Wang T, Xu S and Wang X 2021 In-plane structure domain size of nm-thick $MoSe_2$ uncovered by low-momentum phonon scattering *Nanoscale* **13** 7723–34
[12] Yuan P, Wang R, Tan H, Wang T and Wang X 2017 Energy transport state resolved Raman for probing interface energy transport and hot carrier diffusion in few-layered MoS_2 *ACS Photonics* **4** 3115–29
[13] Wang R, Wang T, Zobeiri H, Yuan P, Deng C, Yue Y, Xu S and Wang X 2018 Measurement of the thermal conductivities of suspended MoS_2 and $MoSe_2$ by nanosecond ET-Raman without temperature calibration and laser absorption evaluation *Nanoscale* **10** 23087–102
[14] Hunter N, Azam N, Zobeiri H, Wang R, Mahjouri-Samani M and Wang X 2020 Interfacial thermal conductance between monolayer WSe_2 and SiO_2 under consideration of radiative electron–hole recombination *ACS Appl. Mater. Interfaces* **12** 51069–81
[15] Zobeiri H, Wang R, Zhang Q, Zhu G and Wang X 2019 Hot carrier transfer and phonon transport in suspended nm WS_2 films *Acta Mater.* **175** 222–37
[16] Hajidavalloo M R, Ayatolah Zadeh Shirazi F and Mahjoob M 2020 Energy cost minimization in an electric vehicle solar charging station via dynamic programming *J. Appl. Comput. Mech.* **51** 275–80
[17] Zobeiri H, Hunter N, Wang R, Liu X, Tan H, Xu S and Wang X 2020 Thermal conductance between water and nm-thick WS_2: extremely localized probing using nanosecond energy transport state-resolved Raman *Nanoscale Adv.* **2** 5821–32
[18] Hunter N, Zobeiri H, Wang T and Wang X 2021 Effect of time and spatial domains on monolayer 2D material interface thermal conductance measurement using ns ET-Raman *Int. J. Heat Mass Transfer* **179** 121644
[19] Wang R, Wang T, Zobeiri H, Li D and Wang X 2020 Energy and charge transport in 2D atomic layer materials: Raman-based characterization *Nanomaterials* **10** 1807
[20] Zobeiri H *et al* 2021 Interfacial thermal resistance between nm-thick MoS_2 and quartz substrate: a critical revisit under phonon mode-wide thermal non-equilibrium *Nano Energy* **89** 106364
[21] Li H, Wu J, Yin Z and Zhang H 2014 Preparation and applications of mechanically exfoliated single-layer and multilayer MoS_2 and WSe_2 nanosheets *Acc. Chem. Res.* **47** 1067–75
[22] Yuan P, Liu J, Wang R and Wang X 2017 The hot carrier diffusion coefficient of sub-10 nm virgin MoS_2: uncovered by non-contact optical probing *Nanoscale* **9** 6808–20
[23] Varshni Y P 1967 Temperature dependence of the energy gap in semiconductors *Physica* **34** 149–54
[24] Sarswat P K and Free M L 2012 A study of energy band gap versus temperature for Cu_2ZnSnS_4 thin films *Physica* B **407** 108–11
[25] Smith E and Dent G 2020 *Modern Raman Spectroscopy: A Practical Approach* (New York: Wiley)
[26] Fan J-H, Gao P, Zhang A-M, Zhu B-R, Zeng H-L, Cui X-D, He R and Zhang Q-M 2014 Resonance Raman scattering in bulk 2H-MX_2 (M= Mo, W; X= S, Se) and monolayer MoS_2 *J. Appl. Phys.* **115** 053527
[27] Loudon R 1963 Theory of the first-order Raman effect in crystals *Proc. R. Soc.* A **275** 218–32
[28] Zobeiri H, Xu S, Yue Y, Zhang Q, Xie Y and Wang X 2020 Effect of temperature on Raman intensity of nm-thick WS_2: combined effects of resonance Raman, optical properties, and interface optical interference *Nanoscale* **12** 6064–78

[29] Huang X *et al* 2016 Quantitative analysis of temperature dependence of Raman shift of monolayer WS_2 *Sci. Rep.* **6** 1–8
[30] Sinha S, Sathe V and Arora S K 2019 Temperature dependent Raman investigations of few-layered WS_2 nanosheets *Solid State Commun.* **298** 113626
[31] Wang T, Xu S, Hurley D H, Yue Y and Wang X 2016 Frequency-resolved Raman for transient thermal probing and thermal diffusivity measurement *Opt. Lett.* **41** 80–83
[32] Zobeiri H, Wang R, Wang T, Lin H, Deng C and Wang X 2019 Frequency-domain energy transport state-resolved Raman for measuring the thermal conductivity of suspended nm-thick $MoSe_2$ *Int. J. Heat Mass Transfer* **133** 1074–85
[33] Conley H J, Wang B, Ziegler J I, Haglund R F, Pantelides S T and Bolotin K I 2013 Bandgap engineering of strained monolayer and bilayer MoS_2 *Nano Lett.* **13** 3626–30
[34] Lu C-P, Li G, Mao J, Wang L-M and Andrei E Y 2014 Bandgap, mid-gap states, and gating effects in MoS_2 *Nano Lett.* **14** 4628–33
[35] O'Hare P A G, Hubbard W N, Johnson G K and Flotow H E 1984 Calorimetric measurements of the low-temperature heat capacity, standard molar enthalpy of formation at 298.15 K, and high-temperature molar enthalpy increments relative to 298.15 K of tungsten disulfide (WS_2), and the thermodynamic properties to 1500 K *J. Chem. Thermodyn.* **16** 45–59
[36] Klemens P G 1958 Solid state physics *Advances in Research and Applications* vol 7 (New York: Academic) p 87
[37] Toberer E S, Zevalkink A and Snyder G J 2011 Phonon engineering through crystal chemistry *J. Mater. Chem.* **21** 15843–52
[38] Huang Z, Wu T, Kong S, Meng Q-L, Zhuang W, Jiang P and Bao X 2016 Enhancement of anisotropic thermoelectric performance of tungsten disulfide by titanium doping *J. Mater. Chem.* A **4** 10159–65
[39] Elahi A, Bidault X and Chaudhuri S 2022 Temperature-transferable coarse-grained model for poly(propylene oxide) to study thermo-responsive behavior of triblock copolymers *J. Phys. Chem.* B **126** 292–307
[40] Zobeiri H, Wang R, Deng C, Zhang Q and Wang X 2019 Polarized Raman of nanoscale two-dimensional materials: combined optical and structural effects *J. Phys. Chem.* C **123** 23236–45
[41] Zobeiri H, Hunter N, Wang R, Wang T and Wang X 2021 Direct characterization of thermal nonequilibrium between optical and acoustic phonons in graphene paper under photon excitation *Adv. Sci.* **8** 2004712
[42] Wang R *et al* 2020 Distinguishing optical and acoustic phonon temperatures and their energy coupling factor under photon excitation in nm 2D materials *Adv. Sci.* **7** 2000097
[43] Liu H-L, Shen C-C, Su S-H, Hsu C-L, Li M-Y and Li L-J 2014 Optical properties of monolayer transition metal dichalcogenides probed by spectroscopic ellipsometry *Appl. Phys. Lett.* **105** 201905
[44] Kim H-C *et al* 2015 Engineering optical and electronic properties of WS_2 by varying the number of layers *ACS nano* **9** 6854–60
[45] Alfihed S, Hossain M, Alharbi A, Alyamani A and Alharbi F H 2013 PLD grown polycrystalline tungsten disulphide (WS_2) films *J. Mater.* **2013** 603648
[46] Beal A R and Hughes H P 1979 Kramers-Kronig analysis of the reflectivity spectra of 2H-MoS_2, 2H-$MoSe_2$ and 2H-$MoTe_2$ *J. Phys. C: Solid State Phys.* **12** 881
[47] Hurley D, Xu S, Wang T, Wang X and Yue Y 2015 Development of time-domain differential Raman for transient thermal probing of materials *Opt. Express* **23** 10040–56
[48] Wang R, Zobeiri H, Lin H, Qu W, Bai X, Deng C and Wang X 2019 Anisotropic thermal conductivities and structure in lignin-based microscale carbon fibers *Carbon* **147** 58–69